Ships and Offshore Structures

ISSN: (Print) (Online) Journal homepage: https://www.tandfonline.com/loi/tsos20

CFD modelling and numerical investigation of a large marine two-stroke dual fuel direct injection engine

Renyou Yang, Gerasimos Theotokatos & Dracos Vassalos

To cite this article: Renyou Yang, Gerasimos Theotokatos & Dracos Vassalos (2022) CFD modelling and numerical investigation of a large marine two-stroke dual fuel direct injection engine, Ships and Offshore Structures, 17:5, 1062-1074, DOI: 10.1080/17445302.2021.1893533

To link to this article: https://doi.org/10.1080/17445302.2021.1893533

Published online: 01 Mar 2021.

SHIPS AND OFFSHORE STRUCTURES
2022, VOL. 17, NO. 5, 1062–1074
https://doi.org/10.1080/17445302.2021.1893533

CFD modelling and numerical investigation of a large marine two-stroke dual fuel direct injection engine

Renyou Yang [a], Gerasimos Theotokatos [b] and Dracos Vassalos [b]

[a]Peng Cheng Laboratory, Shenzhen, People's Republic of China; [b]Maritime Safety Research Centre, Department of Naval Architecture, Ocean and Marine Engineering, University of Strathclyde, Glasgow, UK

ABSTRACT

This study aims at developing a CFD model for large marine two-stroke dual fuel engine with gaseous fuel direct injection at high pressure. For the gaseous fuel, the shock tube theory and the pseudo-diameter concept are employed to model the injection, jet penetration and air entrainment processes, whereas its non-premixed combustion is represented by a steady diffusion flamelet model along with a pilot fuel ignition kernel. Following this model validation, a large marine two-stroke dual fuel engine closed cycle is simulated for both the gas and diesel modes at 75% load, and the involved phenomena are comparatively assessed. The derived results demonstrate that the gas mode combustion takes place in lower maximum temperature and leaner conditions compared to the diesel mode, resulting in lower NOx emissions. This study is expected to benefit the development of future engine designs and the engine settings optimisation for reducing emissions and increasing efficiency.

ARTICLE HISTORY
Received 13 August 2020
Accepted 9 February 2021

KEYWORDS
CFD modelling; marine two-stroke dual fuel engines; high pressure gas direct injection; gas and diesel operating modes

Nomenclature

$C_{P,k}$	specific heat capacity of species k [J/kg/K]
d	diameter [m]
d_n	gas nozzle diameter [m]
dt	time step [s]
F_{Ui}	momentum sources of the injected gas [N/m^3]
$\dot{m}_g$	gas flow rate [kg/s]
P	static pressure [Pa]
P_6	pressure upstream the normal shock [Pa]
r	local radius in the ignition kernel [m]
R_{mg}	universal gas constant [J/kg/K]
R_{ig}	ignition radius [m]
S_h	total enthalpy source [W/m^3]
S_{ig}	energy source of the pilot fuel combustion [W/m^3]
S_k	turbulent kinetic energy source [kg/s^3/m]
S_m	mass source of the fuel vapour [kg/s/m^3]
S_ε	turbulence dissipation rate source [kg/s^4/m]
S_U	mass source of the injected gas [kg/s/m^3]
S_Z	mixture fraction of the injected gas [kg/m^3/s]
S_{Zm}	mixture fraction of the fuel vapour [kg/m^3/s]
T	temperature [K]
$\bar{T}_{ir}$	temperature distribution in the ignition kernel [K]
T_{local}	local temperature in the ignition kernel [K]
T_m	maximum local cylinder temperature [K]
T_r	flame-edge temperature [K]
U_g	gas injection velocity [m/s]
U'_g	gas jet velocity fluctuation [m/s]
V_{ig}	ignition kernel volume [m^3]
$\vec{x}_l$	ignition kernel location [m]
Y_k	species k mass fraction [-]

Greek symbols

ρ	density [kg/m^3]
γ	specific heats ratio
δV_g	pseudo volume of the injected gas jet [m^3]
Ω	engine chamber volume [m^3]

Subscripts

∞	engine combustion chamber
g	injected gas
ps	pseudo-diameter

Abbreviations:

ATDC	after top dead centre
EVO	exhaust valve opening
CA	crank angle
CO	carbon monoxide
CO_2	carbon dioxide
NOx	nitrogen oxides
SOx	sulphur oxides
TDC	top dead centre

1. Introduction

Two-stroke diesel engines are widely used for ocean-going ships propulsion, due to their reliability, cost-effectiveness and efficiency. However, after-treatment systems or alternative fuels are required to ensure the compliance with the current and forthcoming stringent regulatory framework for ships exhaust gas emissions, in specific, the nitrogen oxides (NOx) and sulphur oxides (SOx) emissions (IMO 2018). Compared to conventional marine fuels, such as heavy fuel oil, natural gas is regarded as a feasible alternative, as it reduces the carbon dioxide (CO_2) and NOx emissions, whilst almost eliminates

CONTACT Gerasimos Theotokatos gerasimos.theotokatos@strath.ac.uk Maritime Safety Research Centre, Department of Naval Architecture, Ocean and Marine Engineering, University of Strathclyde, Glasgow G4 0LZ, UK

the SOx and particulate matter (PM) emissions (Kjemtrup 2015; Ott 2015).

Natural gas primarily consists of methane and exhibits high compatibility with the compression-ignition (CI) engines, due to the methane high auto-ignition temperature and anti-knock properties. In this respect, the dual fuel engines with the natural gas directly injected within the engine cylinders (close or after the top dead centre) at high pressure (around 300 bar) constitutes one of the commercially available types of marine two-stroke propulsion engines. The gas fuel combustion is initiated by the injection of the pilot liquid fuel close to the cylinder top dead centre. This engine type delivers the same power output at both the gas and diesel operating modes and avoids knock and misfire issues. Compared to the diesel mode operation, the engine achieves NOx and CO_2 emissions reduced by 25% and 20% respectively, whereas the methane slip is limited. However, an after-treatment system (typically exhaust gas recirculation) is required to achieve compliance with the IMO Tier III NOx regulations.

Douville (1994) conducted an experimental investigation of the combustion and emissions characteristics of a four-stroke dual fuel engine with direct injection of pilot fuel and natural gas at high pressure. It was concluded that this engine operating at the gas mode achieved higher thermal efficiency at high loads and lower pollutant emissions over the entire load range in comparison to the diesel mode operation.

The injection timing of both the pilot and gas fuels affects the engine performance and the associated emissions. Various research studies (Duggal et al. 2014; Larson 2003, Li et al. 2015; Zhang et al. 2015) experimentally quantified the variation of the engine performance and emissions parameters of four-stroke engines with direct gas injection. Larson (2003) investigated the influence of the injection timing and pressure, as well as the exhaust manifold pressure and the boost pressure on the engine exhaust gas emissions. Zhang et al. (2015) demonstrated that the higher combustion quality and engine thermal efficiency were achieved through increasing the gas injection pressure, which was also beneficial for the hydrocarbons (HC) emissions reduction. McTaggart-Cowan et al. (2004) conducted a thorough experimental investigation of a single cylinder four-stroke heavy-duty engine, testing the injection pressure variation with engine speed and load, the gas composition (including ethane, propane and methane), the gas dilution (inert nitrogen) and the hydrogen addition. The effects of these parameters on the engine combustion and emissions characteristics (including efficiency, combustion variability, gaseous fuel ignition delay, combustion duration) were quantified in McTaggart-Cowan et al. (2007) and McTaggart-Cowan et al. (2010). Brown (2008) tested a new injector type, which facilitated first the mixing of the gaseous and the pilot diesel fuels in a dedicated gas-diesel reservoir, and then the pilot-gas fuels mixture injection into the engine cylinder. It was concluded that this injector type affected the combustion repeatability, which was found to be dependent on several parameters including the injected fuels timing and quantities.

A number of studies addressed the modelling of dual fuel engines with direct gaseous fuel injection at high pressure. Ouellette (1996) used the ignition delay derived from the shock-tube experiments (Tsuboi and Wagner 1975) to estimate the methane reaction rate during the ignition delay period, under the assumption of homogeneous conditions and negligible heat diffusion from the ignition locations. The eddy-dissipation model was employed to model the methane non-premixed combustion taking into account the two-step chemical reactions mechanism considering carbon monoxide (CO) as an intermediate combustion product. Li et al. (2005) decoupled the combustion process considering the pilot diesel fuel ignition and combustion as well as the gaseous fuel combustion. The pilot fuel ignition delay was estimated by employing the Shell model (Halstead et al. 1977), which can represent the auto ignition at any combustion conditions except for the purely premixed process. The gaseous fuel combustion was modelled by considering the characteristic-time combustion approach.

Lee and Montgomery (2014) numerically investigated a four-stroke dual fuel engine with natural gas high pressure direct injection (HPDI) by employing the SAGE direct chemistry solver combined with the reduced chemical mechanism developed by Patel et al. (2004). The impact of the relative injection timing (difference between the pilot and gaseous fuels injection start) on the engine indicated mean effective pressure (IMEP) and NOx emissions was identified concluding that the gaseous fuel injection start is the most influencing parameter for the engine combustion control. Li et al. (2017) used the SAGE solver to investigate the hydrogen addition to the gas direct injection dual fuel engine. The CONVERGE CFD software (CONVERGE 2018) indicated that the SAGE solver is used to simulate various combustion modes including premixed, non-premixed, partially premixed and multiple fuels. Wang et al. (2017) investigated the influence of injection profiles and the nozzle angle on the combustion and emissions (NOx and soot) characteristics of a four-stroke dual fuel engine with direct gas injections by employing the AVL-FIRE CFD software and the 3-Zone Extended Coherent Flame Model (ECFM-3Z) (Colin and Benkenida 2004). Gao et al. (2014) investigated by CFD simulations the effect of the gaseous fuel injection pressure on the engine emissions demonstrating that the injection pressure increase results in the NO emissions increase and the HC emissions reduction without significantly affecting the engine performance parameters.

The studies discussed in the preceding paragraphs investigated four-stroke direct injection dual fuel engines. However, the pertinent literature review reveals the lack of numerical and experimental studies focusing on marine two-stroke engines with the exception of a previous authors' study (Yang et al. 2020) that focused on the parametric investigation of the gas injection settings for a marine two-stroke dual fuel engine. Moreover, previous studies did not consider the effects of the expansion waves inside the gas nozzle and the barrel-shaped shocks in the vicinity of the gas nozzle exit on the gas fuel penetration within the engine chamber. This study aims at developing a CFD model to sufficiently represent the processes of the closed cycle of a marine two-stroke engine with direct gaseous fuel injection. To address the previous studies limitations discussed above, the pseudo-diameter concept (Ouellette and Hill 2000) and the one-dimensional shock tube theory (Hajialimohammadi et al. 2016) are combined to

accurately evaluate the gas jet penetration and the air entrainment. In addition, a novel approach for modelling the gas admission in the engine combustion chamber is developed by appropriately calculating the corresponding source terms in the governing equations. Another novel element of this study is the customisation of the steady flamelet model (Peters 1984), which is used to represent the non-premixed combustion of both the injected pilot liquid and gaseous fuels. This combustion model combined with the methane skeleton chemical kinetics according to Bilger and Starner (1990) is incorporated to the ANSYS Fluent CFD software (ANSYS 2015). The pilot fuel injection and combustion processes are first modelled, and subsequently, the developed ignition kernel is employed for the initiation of the natural gas combustion process. The large marine two-stroke engine 5S60ME (MAN Diesel & Turbo 2014; MAN Energy Solutions 2015) is modelled in this study for both the gas and diesel operating modes. The simulation results are analysed to discuss and performance and emissions characteristics comparatively assessing the engine phenomena for both the gas and diesel modes.

2. CFD model description

In the case of marine dual fuel engines with gaseous fuel direct injection, both the pilot liquid and gaseous fuels are injected into the combustion chamber towards the end of the compression process. The pilot liquid fuel injection initiates the processes of spray break up, droplets atomisation, evaporation and air entrainment (mixing of the air and fuel vapour), whilst the pilot fuel combustion commences when the temperature is above the fuel auto-ignition temperature, generating a combustion kernel. Subsequently, the engine main gaseous fuel is directly injected into the engine cylinders, initiating the processes of the gas penetration, the air entrainment (mixing), the preparation of combustible mixture; the latter is ignited by the pilot fuel combustion kernel. In this study, the involved processes for the injection and combustion of both the pilot and gaseous fuels are modelled by developing appropriate models in the ANSYS Fluent software (ANSYS 2015). The engine operation at the diesel mode is also modelled by employing the approach used for the pilot fuel injection and combustion, which is reported in the following paragraphs.

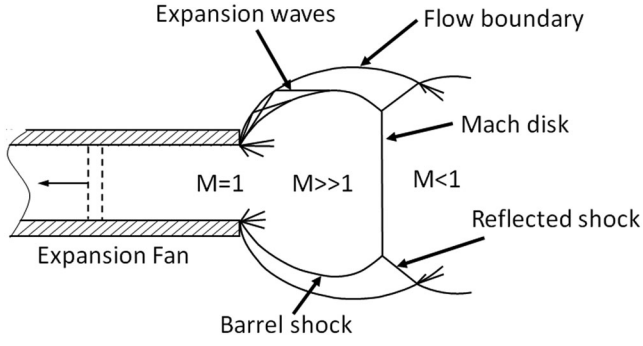

Figure 1. Schematic demonstrating the gas flow phenomena taking place inside the gas nozzle and downstream the nozzle exit (adapted from Ouellette and Hill 2000) (This figure is available in colour online.).

2.1 Pilot fuel injection model

The pilot fuel injection model was developed and customised in ANSYS Fluent (ANSYS 2015). An atomiser model with a cone-shape region was employed to represent the initial state of the injected pilot fuel. A number of parameters are provided as input to this model, including the injection centre, the orifice diameter, the spray axis and angle, as well as the injection pressure. The Bernoulli equation was used to estimate the pilot fuel injection velocity and the associated mass flow rate, considering the orifice pressure drop. The Stochastic Secondary Droplet (SSD) model (Apte et al. 2003) was employed to represent the droplets breakup process.

2.2 Gas injection model

As the gaseous fuel is injected at high-pressure into the engine combustion chamber, the flow phenomena shown in the schematic of Figure 1 are expected to take place. In specific, an underexpanded flow (barrel-shaped pattern) will be formed in the vicinity of the gas nozzle exit (downstream the exit), whereas an expansion fan will be formed inside the gas nozzle. The effects of this barrel-shaped pattern on the downstream flow can be represented by employing the pseudo-diameter concept (Ouellette and Hill 2000). The pressure drop caused by the expansion wave travelling upstream the nozzle (towards the high-pressure side) can be estimated by using the shock tube theory, as reported in Hajialimohammadi et al. (2016).

Based on the shock tube theory applied in the case of one-dimensional compressible flow, and considering the pertinent mass, momentum, energy and the gas state equations (Yang 2018) in conjunction with the pseudo-diameter concept (Ouellette and Hill 2000), the following equations are derived for the calculation of the injected gas velocity U_g and the pseudo diameter d_{ps}:

$$U_g = (P_6 - P_\infty)\sqrt{\frac{2}{\rho_\infty[(\gamma_\infty+1)P_6+(\gamma_\infty-1)P_\infty]}} = \frac{2\sqrt{\gamma_g R_{mg} T_g}}{\gamma_g - 1}\left[1-\left(\frac{P_6}{P_g}\right)^{(\gamma_g-1)/2\gamma_g}\right] \quad (1)$$

$$d_{ps} = d_n\sqrt{\frac{P_6}{P_\infty}} \quad (2)$$

The gas is injected at high-pressure (around 300 bar) into the engine combustion chamber. Considering the combustion chamber pressure (which depends on the engine load), it is deduced that sonic conditions prevail in the gas nozzle. Consequently, the injected gas flow rate $\dot{m}_g$ and the injected gas density ρ_{ps} can be evaluated by the following equations:

$$\dot{m}_g = \frac{1}{4}\pi d_n^2 \rho_g \sqrt{\gamma_g R_{mg} T_g}\left(\frac{2}{\gamma_g+1}\right)^{\frac{2\gamma_g-1}{2(\gamma_g-1)}} \quad (3)$$

$$\rho_{ps} = \rho_g \frac{P_\infty}{P_6}\frac{\sqrt{\gamma_g R_{mg} T_g}}{U_g}\left(\frac{2}{\gamma_g+1}\right)^{\frac{2\gamma_g-1}{2(\gamma_g-1)}} \quad (4)$$

The pressure P_6 in front of the shock wave is calculated by employing Equation (1). Subsequently, the high-pressure gas injection velocity U_g can be evaluated using Equation (1), whereas the pseudo diameter d_{ps}, the gas injection rate $\dot{m}_g$ and the related gas density ρ_{ps} are calculated by using Equations (2)–(4), respectively.

2.3 Continuous phase modelling

The CFD model implemented in ANSYS Fluent employs the Favre-averaged Navier-Stokes equations (Hinze 1975) to represent the gaseous fuel injection and non-premixed combustion processes; these are expressed by the following equations:

$$\frac{\partial \tilde{\rho}}{\partial t} + \frac{\partial}{\partial x_i}(\tilde{\rho}\tilde{u}_i) = S_m + S_U \tag{5}$$

$$\frac{\partial}{\partial t}(\tilde{\rho}\tilde{u}_i) + \frac{\partial}{\partial x_j}(\tilde{\rho}\tilde{u}_i\tilde{u}_j) = -\frac{\partial \tilde{p}}{\partial x_i} + \frac{\partial}{\partial x_j}\left[\mu\left(\frac{\partial \tilde{u}_i}{\partial x_j} + \frac{\partial \tilde{u}_j}{\partial x_i} - \frac{2}{3}\delta_{ij}\frac{\partial \tilde{u}_l}{\partial x_l}\right)\right] + \frac{\partial}{\partial x_j}(-\tilde{\rho}\widetilde{u_i'u_j'}) + \tilde{\rho}g_i + F_{Ui} \tag{6}$$

$$\frac{\partial}{\partial t}(\tilde{\rho}\tilde{H}) + \frac{\partial}{\partial x_i}(\tilde{\rho}\tilde{u}_i\tilde{H}) = \frac{\partial}{\partial x_i}\left(\frac{k_t}{C_p}\frac{\partial \tilde{H}}{\partial x_i}\right) + S_h \tag{7}$$

$$\frac{\partial}{\partial t}(\tilde{\rho}k) + \frac{\partial}{\partial x_i}(\tilde{\rho}k\tilde{u}_i) = \frac{\partial}{\partial x_j}\left(\alpha_k\mu_t\frac{\partial k}{\partial x_j}\right) + G_k + G_b - \tilde{\rho}\varepsilon - Y_M + S_k \tag{8}$$

$$\frac{\partial}{\partial t}(\tilde{\rho}\varepsilon) + \frac{\partial}{\partial x_i}(\tilde{\rho}\varepsilon\tilde{u}_i) = \frac{\partial}{\partial x_j}\left(\alpha_\varepsilon\mu_t\frac{\partial \varepsilon}{\partial x_j}\right) + C_{1\varepsilon}\frac{\varepsilon}{k}(G_k + C_{3\varepsilon}G_b) - C_{2\varepsilon}\tilde{\rho}\frac{\varepsilon^2}{k} - R_\varepsilon + S_\varepsilon \tag{9}$$

$$\frac{\partial}{\partial t}(\tilde{\rho}\tilde{Z}) + \nabla\cdot(\tilde{\rho}\vec{\tilde{v}}\tilde{Z}) = \nabla\cdot\left(\frac{\mu_t}{\sigma_t}\nabla\tilde{Z}\right) + S_{Zm} + S_Z \tag{10}$$

$$\frac{\partial}{\partial t}\left(\tilde{\rho}\widetilde{Z^{2}}'\right) + \nabla\cdot\left(\tilde{\rho}\vec{\tilde{v}}\widetilde{Z^{2}}'\right) = \nabla\cdot\left(\frac{\mu_t}{\sigma_t}\nabla\widetilde{Z^{2}}'\right) + C_g\mu_t\left(\nabla\widetilde{Z^{2}}'\right) - C_d\tilde{\rho}\frac{\varepsilon}{k}\widetilde{Z^{2}}' \tag{11}$$

The conserved-equation sources included in Equations (5)–(11) are used to introduce the high-pressure injected gas into the engine combustion chamber. These sources are represented by the following equations:

$$S_U = \sum \dot{m}_g/\delta V_g \tag{12}$$

$$\vec{F}_U = \sum U_g\dot{m}_g\vec{n}_g/\delta V_g \tag{13}$$

$$S_h = \sum \dot{m}_g\left(\int_{T_{ref}}^{T_g} C_{Pg}dT + h_{0g}\right)/\delta V_g \tag{14}$$

$$S_Z = \sum \dot{m}_g/\delta V_g \tag{15}$$

The volume δV_g at nozzle exit is related to the pseudo diameter, and is calculated by using the following equation

$$\delta V_g = \frac{1}{6}\,\pi\, d_{ps}^3 \tag{16}$$

The RNG k-ε model was employed to simulate the turbulence in the engine combustion chamber. According to Choi et al. (2015), the sources of the turbulence kinetic energy and the dissipation rate in the combustion chamber induced by the high-pressure injected gas at the nozzle exit are calculated by the following equations

$$S_k = 1.5\,(U_g')^2\rho_{ps}/dt \tag{17}$$

$$S_\varepsilon = 0.5[1.5\,(U_g')^2]^{1.5}\rho_{ps}/(d_n\,dt) \tag{18}$$

$$U_g' = 0.12\,U_g \tag{19}$$

Prior to the calculation of the conserved-equation sources, the engine combustion chamber pressure P_∞ needs to be evaluated for the estimation of the injected gas velocity and mass flow rate as well as the pseudo diameter. This is realised by using the following equation

$$P_\infty = \frac{\iiint_\Omega \tilde{\rho}\tilde{P}dV}{\iiint_\Omega \tilde{\rho}dV} \tag{20}$$

The integration of the developed model for the calculation of the gaseous fuel injection processes and the main ANSYS Fluent CFD model is described in Figure 2.

2.4 Combustion model

According to the non-premixed combustion concept, it is considered that the fuel and the oxidiser streams are independently introduced into the combustion chamber. For the case of the marine two-stroke engine, the pilot liquid fuel is firstly injected into the combustion chamber close to the cylinder top dead centre, which initiates the combustion and generates an ignition kernel for the combustion of the gaseous fuel. Subsequently, the gaseous fuel is directly injected at high-pressure and it mixes with the entrained air forming a combustible mixture, which is ignited by the pilot fuel ignition kernel. This study assumes that the combustion processes can be decoupled into the following two parts: pilot fuel combustion, and main gaseous fuel combustion.

2.4.1 Pilot fuel combustion model

The pilot fuel combustion model is based on the laminar flamelet concept, which was introduced by Murthy (1974) and further developed by Peters (1984). The effects of the realistic chemical kinetics on the turbulent flames are included in this diffusion flamelet model.

A probability density function (PDF) of the β-function – type is employed for the estimation of the turbulence-chemistry interactions. The pilot fuel is considered to be n-heptane. The model considers 28 species whilst the skeleton chemical kinetics in the laminar flamelet includes 52 chemical reactions (ANSYS 2015).

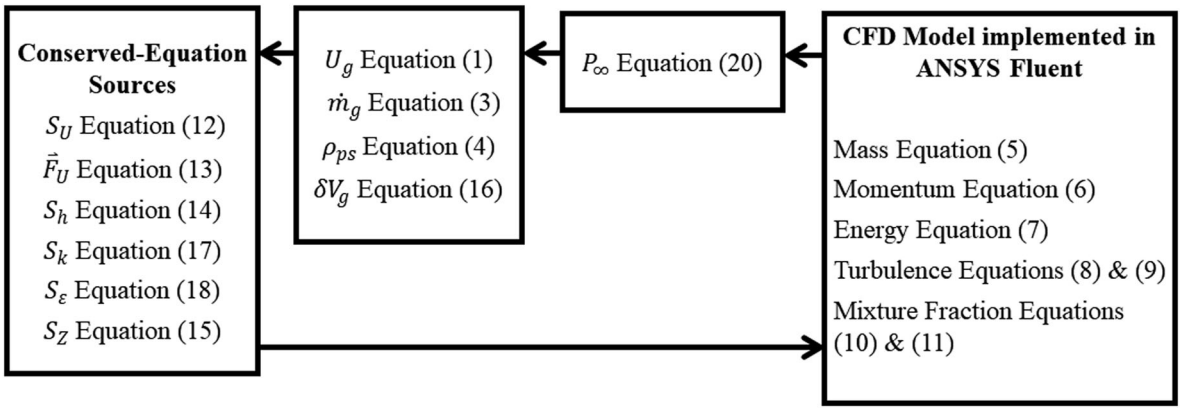

Figure 2. The interaction between the gas injection model and the CFD models (This figure is available in colour online.).

The pilot fuel combustion aims to obtain the characteristics of the ignition kernel, including the location, the radius and the temperature distribution. By using the predicted temperature distribution, the associated ignition location $\vec{x}_l$, the radius R_{ig} and the temperature distribution $\bar{T}_{ir}$ within the ignition kernel are estimated according to the following equations:

$$\vec{x}_l = \frac{\iiint_{V_{ig}} \vec{x}_l \rho dV}{\iiint_{V_{ig}} \rho dV} \tag{21}$$

$$R_{ig} = \sqrt[3]{\frac{3}{4\pi} V_{ig}} \tag{22}$$

$$\bar{T}_{ir} = \frac{r}{R_{ig}}(T_m - T_r),\ r \in [0,\ R_{ig}] \tag{23}$$

2.4.2 Gaseous fuel combustion model

As the gaseous fuel is directly injected at high-pressure into the combustion chamber and subsequently mixed with the combustion chamber working medium (mostly air), the ignition kernel generated by the pilot fuel is employed to initiate the combustion of the gaseous fuel–air mixture. The combustion is dominated by a limited mixing process and the diffusion flame concept. Hence, the gaseous fuel combustion is modelled by employing the steady diffusion flamelet model considering a single mixture fraction approach (Peters 1984).

Taking into account the location, the radius and the temperature distribution of the ignition kernel calculated by equations (21–23), the energy-equation source attributed to the pilot fuel combustion is estimated by the following equation:

$$S_{ig} = \sum_k Y_k \left[\int_{T_{\text{local}}}^{\bar{T}_{ir}} C_{P,k} dT \right] \tag{24}$$

The gaseous fuel is considered to be methane, whereas the combustion model considers 17 species and 58 chemical reactions, as reported in Bilger and Starner (1990). The steady diffusion flamelet model steps are illustrated in the flowchart of Figure 3. The model employs the generation of parameters look-up tables to reduce the model computational effort. The methane combustion mechanism considering two-dimensional counterflow laminar flamelet is employed, and then integrated and tabulated by using the β-shaped probability density function (PDF) to represent the interactions between the fuel combustion and turbulence. The scalar dissipation rate χ is introduced into the look-up table to account for the effects of the flow strain in the steady diffusion flamelet.

2.5 NOx formation model

NOx formation takes place at the non-equilibrium conditions, and is strongly affected by the temperature. As the NOx production rate is much lower than the fuel burning rate, the NOx formation generally can be considered as a post process of the fuel combustion.

As the NOx emissions mainly consist of nitric monoxide (NO), the developed model employs the following two NO mechanisms: the extended Zeldovich mechanism, and the NO formation mechanism from intermediate N_2O. For the extended Zeldovich mechanism, the forward and the reverse rates of the NO reaction equations are considered as reported by Hanson and Salimian (1984). The rates for the NO formation from the intermediate N_2O is taken according to Melte and Pratt (1974); this mechanism is relatively significant in the high pressure ranges and oxygen-rich conditions.

3. Developed CFD model validation

The developed CFD model was validated against the previous published experimental measurements reported in Imhof et al. (2013), which are taken for both the gas and the diesel operating modes in a rapid compression and expansion machine (RCEM) [40], the characteristics of which are presented in Table 1. The CFD model employed the n-heptane as the pilot fuel at the gas mode and the main fuel at the diesel mode, whereas the gaseous fuel (for the gas mode) is considered to be methane. In addition, the RNG k-ε turbulence model is used, whereas adiabatic conditions are assumed. Figure 4 shows the used mesh at the top dead centre (TDC) of the RCEM. Following a mesh size study and taking not account the trade-off between the results accuracy and simulation computational cost, the mesh size of 1 mm was selected, as it provided an effective representation ofboth the gaseous and liquid fuels injection processes (Yang 2018).

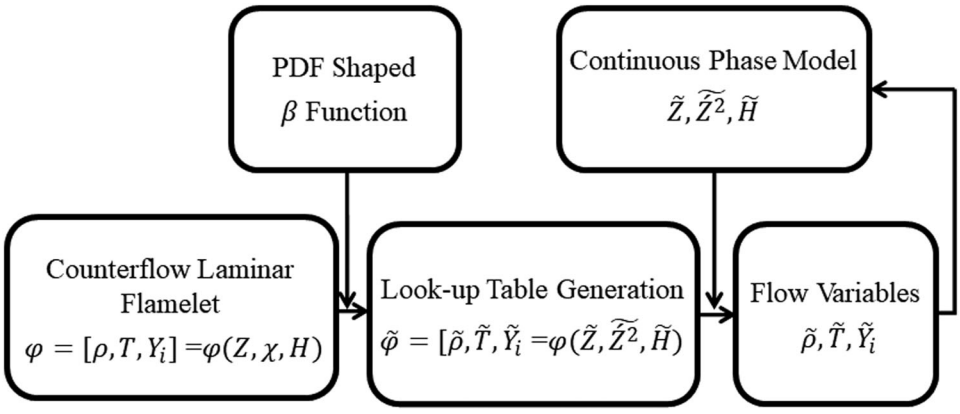

Figure 3. Flowchart of the steady diffusion combustion model calculation procedure (This figure is available in colour online.).

Figure 5 presents the heat release rate (HRR) calculated by the developed CFD model and from the available experimental data published in Imhof et al. (2013), for both the gas and diesel operating modes. The respective HRR values at 0°ATDC and 15°ATDC as well as the NO emissions are presented in Table 2. At the early combustion process stage, the CFD model results perfectly match the experimental data; the gas mode combustion exhibits a steeper rise of HRR compared to the gas mode. At the late combustion stage, the CFD model slightly overpredicted the HRR for the gas mode and underestimated the HRR for the diesel mode. The noticeable peak of the HRR variations for the diesel and gas modes are sufficiently captured by the developed CFD model. As it is shown in Table 2, the derived relative errors for both modes are within 9%; the gas mode results exhibited the higher errors. However, considering the typical errors ranges expected in CFD modelling, it can be deduced that the developed CFD model can adequately represent the combustion processes in both the gas and diesel modes.

The reaction rates in the extended Zeldovich mechanism recommended by Hanson and Salimian (1984) were employed to evaluate the NO emissions. The results shown in Table 2 demonstrate that the NOx emissions are reduced by 26% for the gas mode in comparison to the diesel mode. This trend was captured by the developed dual fuel non-premixed combustion model, despite of the noticeable discrepancy between the predicted and measured values. The results also indicated that the prediction of NO emissions exhibit a relatively high error (up to 38% for the gas mode). Schwerdt (2006) and Tao et al. (2007) reported that the errors of NO emissions evaluated by the extended Zeldovich mechanism can reach 50% or above.

Table 1. Rapid compression and expansion machine (RCEM) characteristics for the diesel and the gas operating models adopted from Imhof et al. (2013).

Diesel Mode		Gas Mode	
Nozzle Hole Diameter (mm)	0.5	Pilot Nozzle Hole Diameter (mm)	0.16
Injection Pressure (MPa)	100	Pilot Injection Pressure (MPa)	60
Injection Start/End (° ATDC)	−5.0/ 18.0	Pilot Injection Start/End (° ATDC)	−7.5/2.8
		Gas Nozzle Hole Diameter (mm)	1.2
		Gas Injection Pressure (MPa)	30
		Gas Injection Start/End (° ATDC)	−6.0/ 18.0

4. Large marine two-stroke engine CFD model results

Following the validation of the developed CFD model, the closed cycle of the large marine two-stroke marine engine 5S60ME [30, 31] at 75% load was modelled for both the diesel and the gas operating modes. The main characterises of this engine are listed in Table 3. The load was selected as representative of the most frequent engine operation. The injectors characteristics for both the gas mode (pilot liquid and gaseous fuels injectors) as well as for the diesel mode (diesel fuel injectors) are presented in Table 4. The injectors characteristics for the gas mode were derived following the parametric investigation reported in the previous authors' study (Yang et al. 2020), whereas the injectors characteristics for the diesel mode are taken from Jin (2014).

The mesh size of 1 mm was selected for the space underneath the exhaust valve, whereas the mesh of the space above the moving piston was generated by employing the spring-deformed mesh concept. The used mesh for the cylinder TCC is shown in Figure 6. The CFD model employs various time steps depending on the modelled process. A time step of 0.1°CA was used for the compression phase (before the pilot fuel injection) and the late expansion phase (after 40°ATDC). A time step of 0.001°CA was used for the pilot liquid and the gaseous fuels injection processes. The gaseous fuel combustion process was modelled with a time step of 0.01°CA time step.

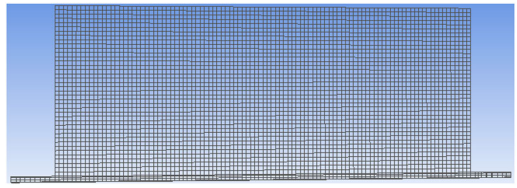

Figure 4. Mesh at top dead centre used for the CFD modelling of the rapid compression and expansion machine (RCEM) processes (This figure is available in colour online.).

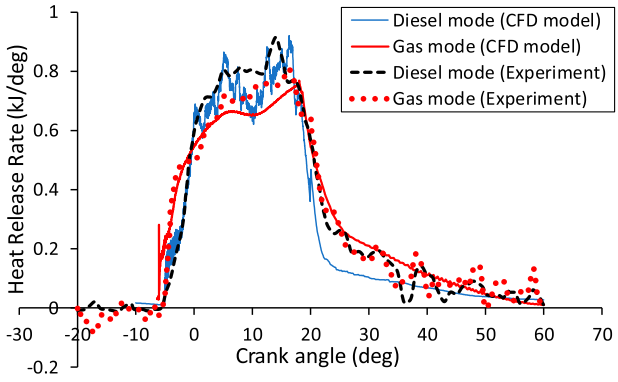

Figure 5. Heat release rates derived from the CFD model and the experimental data reported in Imhof et al. (2013) for the diesel and gas operating modes for the rapid compression and expansion machine (RCEM) (This figure is available in colour online.).

4.1 Temporal and spatial distributions on the flame structure

The local in-cylinder fuel–air equivalence ratio versus the temperature at crank angle values equal to 0.0°ATDC, 5.07° ATDC, 10.07°ATDC and 15.07°ATDC for the gas and the diesel modes, respectively are illustrated in Figure 7. For both modes, the diffusion combustion that is linked to the high temperature region takes place at lean conditions. At the same temperature, the gas mode exhibits a broader equivalence ratio distribution compared with the diesel mode. It is inferred that a greater flammability limit is obtained due to the combustion at rich conditions for the gas mode. For the same equivalence ratio, a higher temperature is exhibited at the gas mode compared with the diesel mode.

The temperature distributions at various crank angles for the gas and diesel modes are shown in Figures 8 and 9. These results demonstrate that the diesel mode (where liquid diesel fuel is burned) exhibits a higher flame temperature than the gas mode, which primarily uses the methane as fuel (the combustion of which is initiated by the injection a pilot fuel amount). At the early gas injection stage, higher flame temperature levels are observed in the gas mode compared with that of the diesel mode, which is attributed to the pilot fuel combustion. Moreover, the locations of the flame temperature for these two investigated operating modes are quite different. For the diesel mode, the diffusion flame is strongly transported by the swirling flow within the cylinder, similarly to the flame developed in the gas mode after the end of the gas injection. However, during the gas injection process for the gas mode, the high-temperature flame is observed primarily in the space of the gas-plume fronts shown in Figure 8.

Table 3. Investigated engine characteristics adopted from (MAN Diesel & Turbo 2014; MAN Energy Solutions 2015).

Parameter	Unit	–
Stoke	m	2.4
Bore	m	0.6
Crank Radius	m	1.2
Engine Speed (75% Load)	rpm	91.3
Engine Power (75% Load)	kW	7875

Table 4. Injectors characteristics for the gas and diesel mode.

	Gas Mode		Diesel Mode
Parameter	Pilot fuel injectors	Gaseous fuel injectors	Diesel fuel injectors
Injectors number	3	3	2
Injector holes number	5	5	5
Injected fuel (kg/rev)	0.00193	0.038	0.0472
Injection start (° ATDC)	−1.5	0	−0.9
Injection end (° ATDC)	3.02	11.24	15.1

4.2 Engine performance parameters

The predicted in-cylinder pressure variations against the crank angle are shown in Figure 10. In addition, the experimentally measured pressure variation for the diesel mode reported in Jin (2014) is also presented in this figure. Experimental results were not available for the gas mode operation. The predicted in-cylinder pressure adequately matches the experimental results, although the model underestimated the maximum cylinder pressure at the diesel mode by 1.8% (compared with the measured data), as shown in Table 4. The predicted indicated mean effective pressure (IMEP) for the engine cylinder closed-cycle was found within 0.1% from its respective experimental value.

By comparing the pressure variations for the gas and the diesel modes (Figure 10 and Table 5), it is deduced that the maximum in-cylinder pressure for the gas mode is slightly higher by 2.2% and is achieved 3°CA earlier than that of the diesel mode. This is attributed to the fact that the combustion at the gas mode starts slightly earlier and it takes place slightly faster in its initial phase compared with the combustion at the diesel mode. After the gas injection, the in-cylinder pressure reduces faster (in the gas mode), whereas the in-cylinder pressure variations (at both modes) almost coincide at the late expansion phase. Nonetheless, the predicted IMEP exhibits almost the same value for both the gas and diesel modes.

Table 2. Comparison of CFD model results and experimental data for the gas and diesel modes for the rapid compression and expansion machine (RCEM).

	CFD model		Experimental data taken from [40]			
	Diesel mode	Gas mode	Diesel mode	Gas mode	Diesel mode	Gas mode
	Heat Release Rate					
CA (°ATDC)	HRR (kJ/°CA)		HRR (kJ/°CA)		Relative Error (%)	
0	0.60	0.54	0.59	0.50	1.7	8.6
15	0.85	0.72	0.85	0.76	0.1	−5.3
NO emissions						
NO (ppm)	648	244	531	346–393	22	(−37.9)–(−29.5)

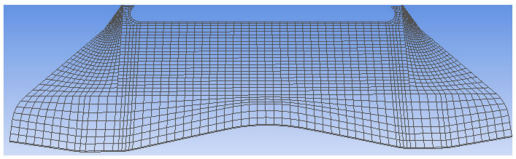

Figure 6. Mesh at top dead centre used for the CFD modelling of the investigated marine two-stroke engine (This figure is available in colour online.).

Figure 11 shows the predicted heat release rates (HRR) for both the gas and diesel modes. For the gas mode, the HRR increases till its maximum value that is achieved at 5.62° ATDC, and then gradually decreases. This is attributed to the fact that the flame front impinges with the cold root of the gas plumes (in the space close to the gaseous fuel nozzles) as it is illustrated from plots shown in Figure 8. Nonetheless, the HRR at the gas mode slightly exceeds the one of the diesel mode in the late combustion phase (after 20°CA) due to the slower combustion of the gaseous fuel. For the diesel mode, the HRR variation exhibits two peaks (with one valley between them) and is remarkably different than that of the gas mode, as shown in Figure 11. The HRRs (for both the diesel and gas modes) abruptly increases till their first peak (observed at 6° ATDC); the gas mode HRR slightly exceeds the respective gas mode HRR due to the earlier start of the pilot fuel combustion (which results in a higher cylinder pressure at the gas mode), whilst the HRR peak value is almost the same to that of the diesel mode. The subsequent reduction of the HRR is attributed to the lower fuel vapour as shown in Figure 12. For the diesel mode, the HRR increases after 9°ATDC, obtaining its second peak (maximum value) at 11.3°ATDC; this is attributed to the increase of the in-cylinder diesel vapour and the associated flame temperature (as inferred from the respective increase of the maximum temperature) as illustrated in Figure 13.

4.3 Gas emissions

The predicted emissions for the investigated engine operating point are shown in Table 6. It is demonstrated from these results that there was no unburned hydrocarbons (HC) left after the combustion for both the gas and diesel modes. However, it must be noted that the in-cylinder crevices and the cylinder lubricating oil film, which impact the unburned HC emissions were not included in the model. Due to the lower methane carbon to hydrogen ratio (compared to the diesel fuel), the CO_2 emissions were significantly lower than that produced for the diesel mode. For the investigated operating point (75% load), the working medium of each engine cylinder contains 0.115 kg CO_2 at the exhaust valve opening (EVO) point in the gas mode, which was 21% lower than CO_2 emissions for the case of the diesel mode.

The predicted NO emissions at the EVO for the gas mode was 1820 ppm (mass fraction), which was 30.6% lower than the NO emissions predicted for the diesel mode. The NO formation depends on the in-cylinder temperature. According to Figure 15, the maximum temperature for the gas mode was remarkably lower for a considerable part of the combustion process, compared to that of the diesel mode. This in conjunction with the leaner combustion conditions (higher equivalence ratio) resulted in the reduction of the NO emissions in

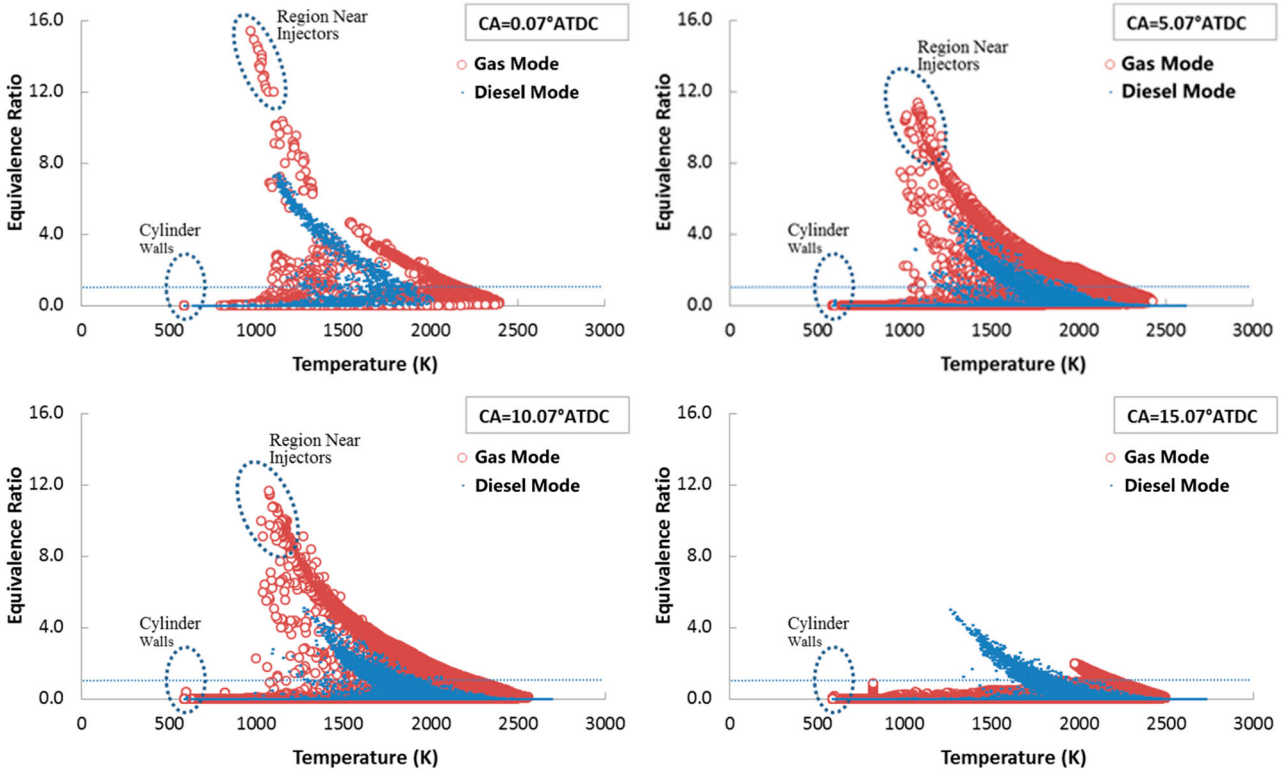

Figure 7. Variation of the local temperature versus equivalence ratio for various crank angles (This figure is available in colour online.).

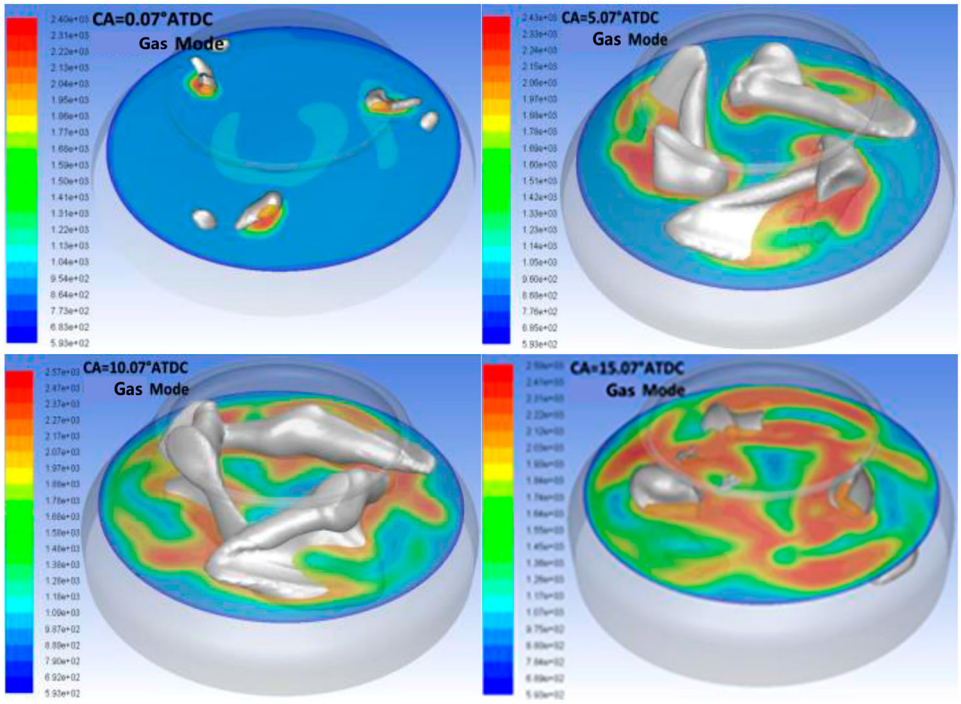

Figure 8. In-cylinder temperature spatial distributions at various crank angles for the gas mode (This figure is available in colour online.).

the gas mode. The predicted CO emissions at the EVO for the gas mode was 4 ppm.

The spatial distributions of the mixture fractions as well as the species OH, CH_2O and CO_2 for the gas and diesel modes are illustrated in Figures 14 and 15. The radical OH denotes the high temperature reaction zones related to the diffusion flame, whereas the CH_2O denotes the low temperature reaction zones. The mixture fraction exhibits a similar distribution with the CO_2. The cores of the gas/vapour plumes exhibit a low OH fraction and a high CH_2O concentration, which is more pronounced close to the nozzles exit. Regarding the high OH and low CH_2O zones, a noticeable disparity between the gas and the diesel operating modes is found. For the gas mode, due to the diffusion combustion of the injected gas, the high-temperature flame is located in the vicinity of the stoichiometric surface; this surface exhibits high concentration

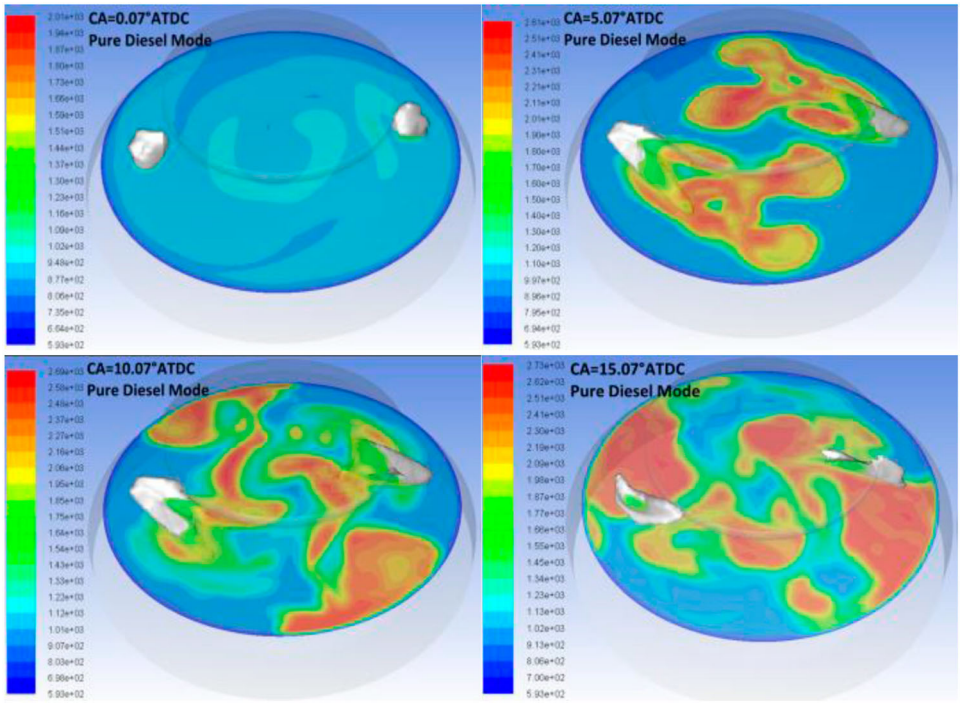

Figure 9. In-cylinder temperature spatial distributions at various crank angles for the diesel mode (This figure is available in colour online.).

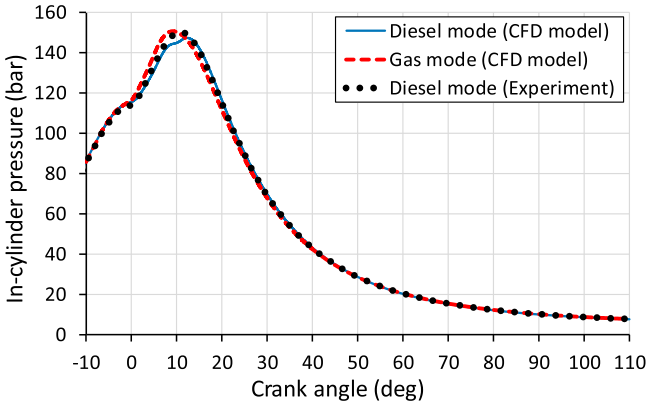

Figure 10. In-cylinder pressure variations for the gas and diesel modes (This figure is available in colour online.).

Table 5. In-cylinder maximum pressure and crank angle for the gas and diesel modes.

		In-cylinder Maximum Pressure	
	Mode	CA at maximum pressure (°ATDC)	Pressure (bar)
CFD model	Diesel	12.4	147.3
Experiment	Diesel	11	150.1
CFD model	Gas	9.1	150.7

of the OH radical and low concentration of the CH_2O. On the contrary, the high CH_2O concentration occurs near the stoichiometric surface for the diesel mode, which is owing to the heat transfer due to the liquid fuel evaporation. Therefore, the high-concentration zones for the OH are not observed close to the stoichiometric surface of the fuel vapour, but downstream the vapour plumes, due to the transportation by the strong swirling flow and the high-speed liquid sprays. In terms of the mixture fraction distribution shown in Figure 14, the slight accumulation of the gas fuel and the related products near the cylinder walls is mainly caused by the hot front of one gas plume impinging on the root of another gas plume.

5. Conclusions

This study aimed at developing and validating a CFD modelling approach for the simulation of large marine two-stroke

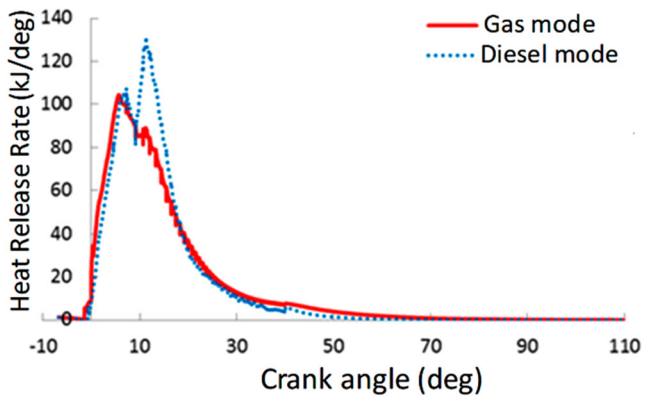

Figure 11. Heat release rate (HRR) curves calculated by the CFD model for the gas and the diesel modes (This figure is available in colour online.).

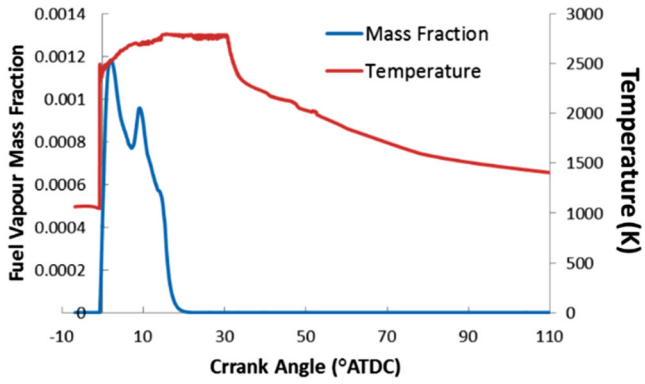

Figure 12. Calculated diesel vapour mass fraction and the in-cylinder maximum temperature for the diesel mode (This figure is available in colour online.).

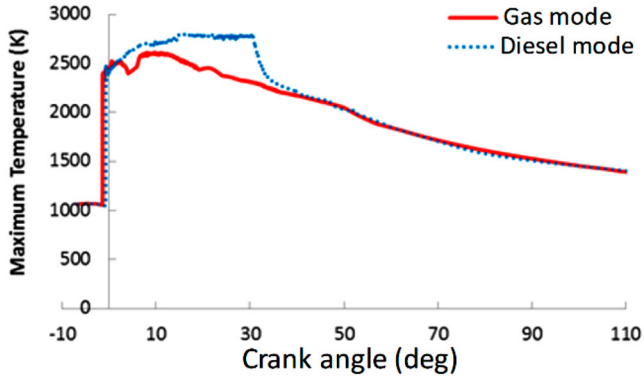

Figure 13. Calculated Maximum in-cylinder temperature for the gas and diesel modes (This figure is available in colour online.).

dual fuel engine with gaseous fuel direct injection at high pressure. The developed model included submodels for representing all the involved process, in specific the pilot liquid fuel injection and combustion as well as the gaseous fuel injection and combustion; this model was incorporated in the commercial CFD software ANSYS Fluent. The developed CFD model was first validated based on the previous published results obtained in a rapid compression and expansion machine (RCEM) (Imhof et al. 2013). Subsequently, the closed cycle of the large marine two-stroke dual fuel engine 5S60ME was simulated for both the gas the diesel operating models considering the operation at 75% load. The derived in-cylinder pressure variations were validated against respective experimental data, whilst a number of performance and emission parameters for both operating modes are comparatively assessed to delineate the involved phenomena taking place within the engine closed cycle. The main findings of this study are summarised as follows:

- The developed CFD model sufficiently represented the RCEM processes of both the gas and diesel modes. The

Table 6. Predicted emissions mass for the gas and diesel modes.

	Unburned HC	CO_2 (%)	NO (ppm)
Gas Mode	None	7.95	1820
Diesel Mode	None	9.96	2622

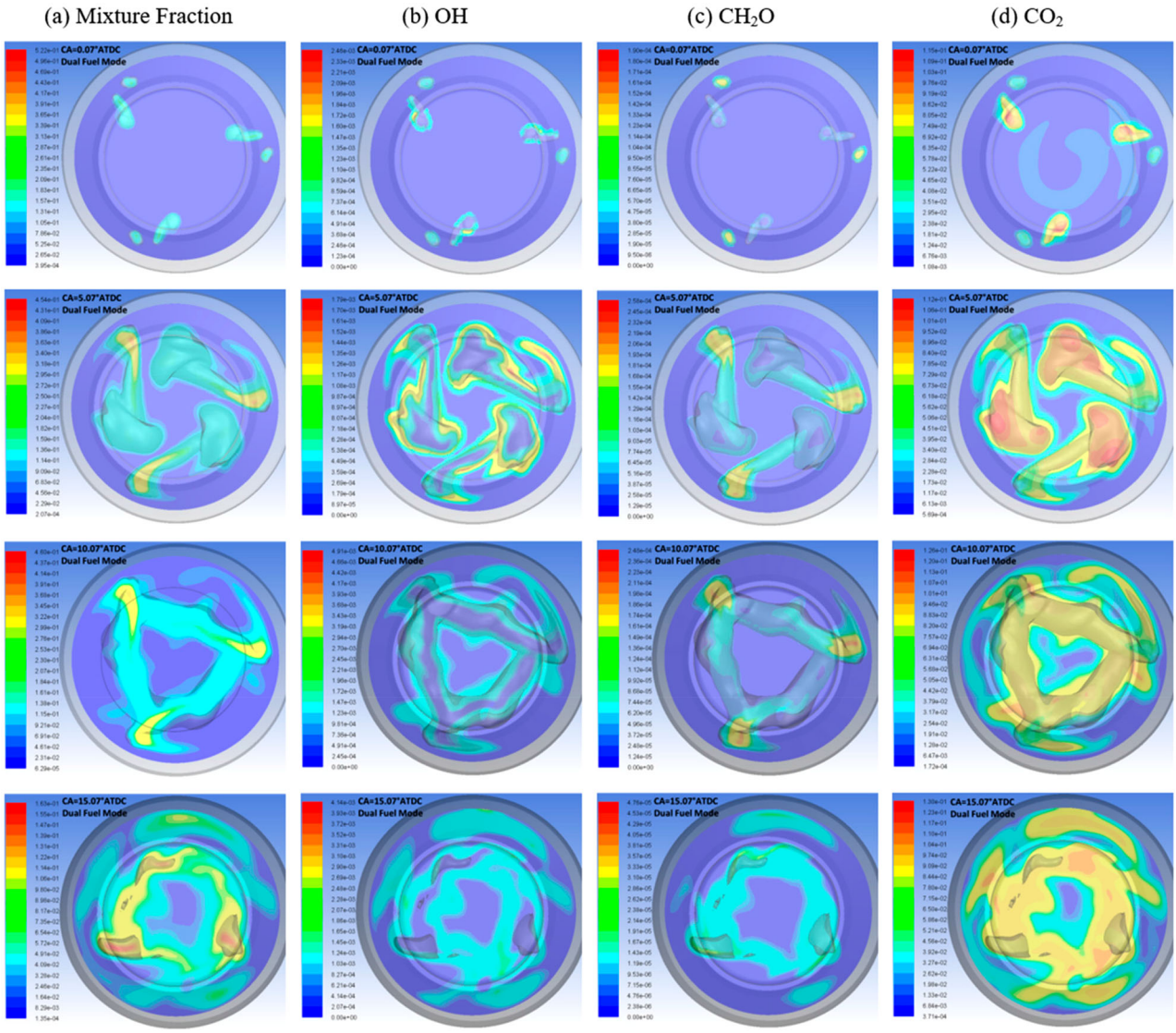

Figure 14. Spatial distributions of mixture fraction, OH, $CH_2O$and CO_2 for the gas mode (This figure is available in colour online.).

HRR deviation between the CFD and experimental results was calculated to be less than 9%. The percentage error in the NO emissions prediction was found up to 38%, which is within the error range reported in the pertinent literature (Schwerdt 2006; Tao et al. 2007).

- The predicted in-cylinder pressure variations and IMEP for the investigated marine two-stroke dual fuel engine operation at 75% load sufficiently matched the respective experimental results for both the gas and diesel modes. The percentage error (between the derived results and the experimental measurements) for the cylinder maximum pressure was found within 1.8%, whereas the closed cycle IMEP relative error was calculated within 0.1%.
- At the gas mode, the cylinder maximum pressure was slightly higher and achieved in a slightly earlier crank angle compared with the diesel mode. However, the engine achieved almost the same IMEP in both operating modes.
- By comparing the derived CFD model results for the cases of the gas and diesel operating modes, it was concluded that the combustion process at the gas mode achieved a lower maximum temperature compared to the diesel mode. Atthe diesel mode, the flame front was found to be in areas with high-temperature, whilst, for the gas mode, the flame front was found to be in the vicinity of the stoichiometric surface.
- For the diesel mode, the heat release rate variation (versus crank angle) was found remarkably different than that of the gas mode. The HRR of the gas mode exhibited a single peak, whereas two peaks were observed in the HRR of the diesel mode. For the period till the first peak, the HRR exhibited similar variations (with only slight differences attributed to the pilot fuel combustion and faster combustion of the gaseous fuel). The HRR was found depended on the fuel vapour retained within the engine combustion chamber. For the late combustion period, the HRR in the gas mode slightly exceeded the one of the diesel mode revealing a slower combustion rate.
- The CFD model results demonstrated that no unburned hydrocarbons were remained at the exhaust valve opening. At the gas mode, the CO_2 and NOx emissions was

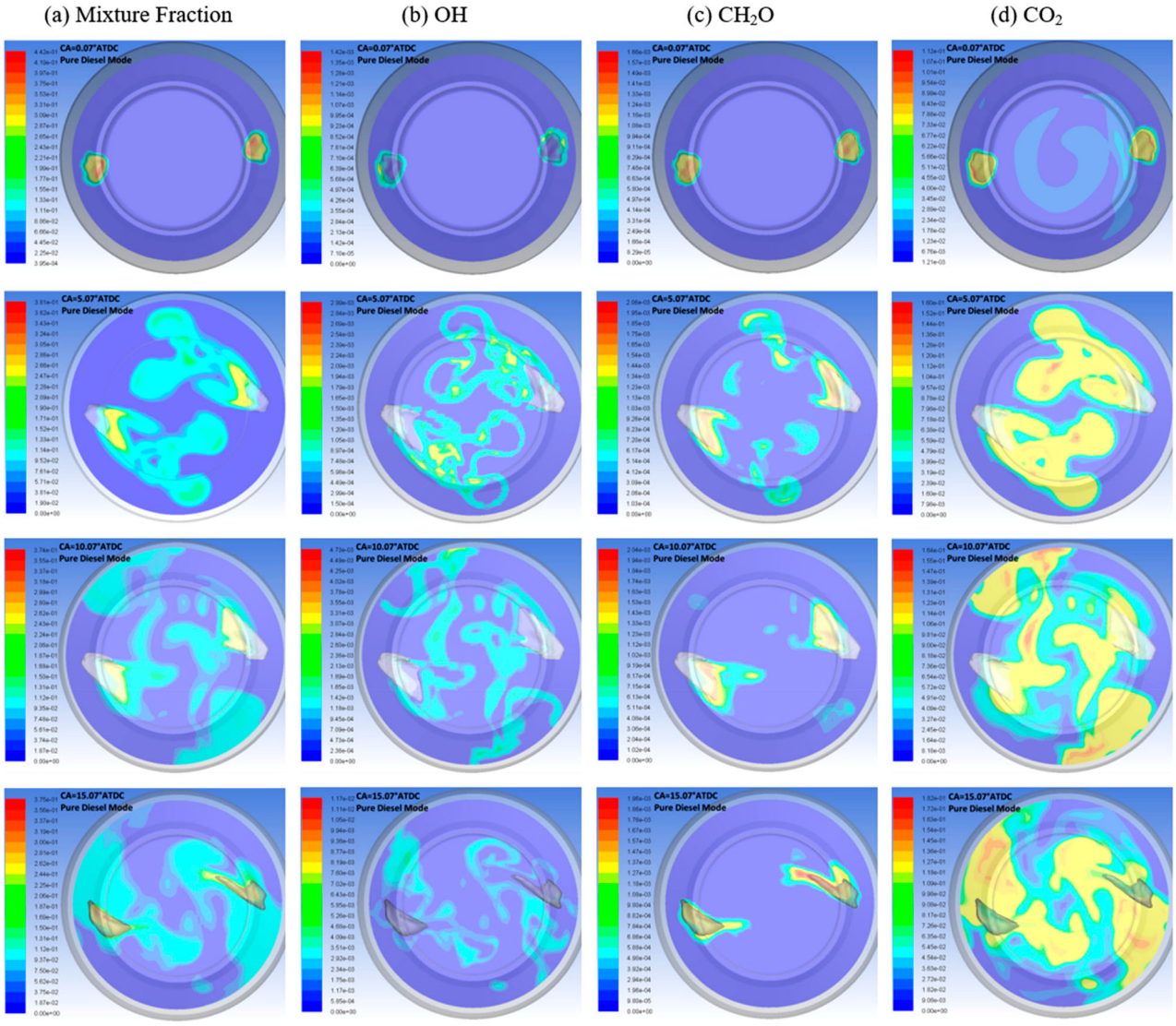

Figure 15. Spatial distributions of mixture fraction, OH, $CH_2O$and CO_2 for the diesel mode (This figure is available in colour online.).

calculated 21% and 30.6% lower, respectively, compared with the diesel mode. These values are in accordance with the respective values reported in the pertinent literature.

The developed modelling approach is novel as it included several innovative methods, in specific, the incorporation of the pseudo-diameter concept, the one-dimensional shock tube theory and the calculation of the required source terms for the representation of the gaseous fuel injection process, the customisation of the steady flamelet model to represent the non-premixed combustion of both the pilot liquid and gaseous fuels, as well as the development of the pilot fuel ignition kernel and its use for the gaseous fuel combustion initiation. In addition, the CFD modelling of the marine two-stroke dual fuel engine with gaseous fuel direct injection is a useful addition in the pertinent literature, which lack of similar studies. Although, this study modelled a two-stroke engine, the developed CFD modelling approach is applicable for the simulation of marine dual fuel four-stroke engines with gaseous fuel direct injection. Moreover, this study results contributes to the better understanding of the phenomena and physical processes taking place in large marine two-stroke engines with gaseous fuel direct injection. Considering the focus of the shipping industry on the reduction of its operations environmental footprint, which can be achieved using LNG or other alternative fuels, it is expected to be beneficial for the development of future engine designs as well as the optimisation of the engine settings targeting to reduce emissions and increase efficiency. These topics will be investigated in future research studies.

Acknowledgements

All the CFD simulations presented in the paper are operated on the ARCHIE-WeSt supercomputers. The authors would like to appreciate the administrators to provide the adequate computational resources to complete this investigation. The authors from MSRC greatly acknowledge the funding from DNV GL AS and RCCL for the MSRC establishment and operation. The opinions expressed herein are those of the authors and should not be construed to reflect the views of DNV GL AS and RCCL.

Disclosure statement

No potential conflict of interest was reported by the author(s).

ORCID

Renyou Yang http://orcid.org/0000-0003-0388-9426
Gerasimos Theotokatos http://orcid.org/0000-0003-3547-8867
Dracos Vassalos http://orcid.org/0000-0002-0929-6173

References

ANSYS. 2015. ANSYS Fluent user guide release 15.0. [accessed 2020 Sep 12]. https://www.ansys.com/

Apte SV, Gorokhovski M, Moin P. 2003. LES of atomizing spray with stochastic modelling of secondary breakup. Int J Multiphase Flow. 29:1503–1522.

Bilger RW, Starner SH. 1990. N-reduced mechanism for methane-air combustion in non-premixed flames. Combust Flame. 80:135–149.

Brown BS. 2008. High-pressure direct-injection of natural gas with entrained diesel into a compression-ignition engine [dissertation]. Vancouver (CA): The University of British Columbia.

Choi M, Lee S, Park S. 2015. Numerical and experimental study of gaseous fuel injection for CNG direct injection. Fuel. 140:693–700.

Colin O, Benkenida A. 2004. The 3-zones extended coherent flame model (ECFM3Z) for computing premixed/diffusion combustion. Oil Gas Sci Technol – Rev. IFP. 59(6):593–609.

CONVERGE. 2018. CFD Software. Internal combustion engines. [accessed 2020 Dec 20]. https://convergecfd.com/applications/internal-combustion-engines.

Douville B. 1994. Performance, emissions and combustion characteristics of natural gas fuelling of diesel engines [dissertation]. Vancouver (CA): The University of British Columbia.

Duggal VK, Lyford-Pike EJ, Wright JF. 2014. Development of the high-pressure direct-injected, ultralow-NOx natural gas engine. Final report. Golden (CO): National Renewable Energy Laboratory (US); May 2004. Report no. NREL/SR-540-35911.

Gao Y, Li X, Li J. 2014. Numerical simulations of natural gas injection pressure effects on a direct injected, pilot ignited, natural gas engine. Appl Mech Mater. 510:179–184.

Hajialimohammadi A, Edgington-Mitchell D, Honnery D, Montazerin N, Abdullah A, Agha Mirsalim M. 2016. Ultra high speed investigation of gaseous jet injected by a single-hole injector and proposing of an analytical method for pressure loss prediction during transient injection. Fuel. 184:100–109.

Halstead MP, Kirsch LJ, Quinn CP. 1977. The autoignition of hydrocarbon fuels at high temperatures and pressures—fitting of a mathematical model. Combust Flame. 30:45–60.

Hanson RK, Salimian S. 1984. Survey of rate constants in H/N/O systems. In: Gardiner WC, editor. Combustion chemistry. Boston, MA: Springer; p. 361–421.

Hinze IO. 1975. Turbulence. 2nd ed. New York: McGraw-Hill.

Imhof D, Tsuru D, Tajima H, Takasaki K. 2013. High-pressure natural gas injection (GI) marine engine research with a rapid compression expansion machine. In: CIMAC Congress 2013: 27th CIMAC World Congress on Combustion Engines; 13-26 May; Shanghai, China.

IMO. 2018. Revised MARPOL Annex VI. International Maritime Organisation. [accessed 2020 Dec 20]. http://www.imo.org/en/OurWork/Environment/PollutionPrevention/AirPollution/Pages/AirPollution.aspx.

Jin W. 2014. CFD modelling and validation of a large two-stroke marine diesel engine [dissertation]. Glasgow (UK): University of Strathclyde.

Kjemtrup N. 2015. Gas two-stroke marine engine design and operation. CIMAC discussion Athens. Jan 2015. [accessed 2020 June 20]. http://www.lme.ntua.gr:8080/whats-new/news-1/G2X_Presentations.pdf.

Larson CR. 2003. Injection study of a diesel engine fuelled with pilot-ignited, directly-injected natural gas [dissertation]. Vancouver (CA): The University of British Columbia.

Lee WG, Montgomery D. 2014. Numerical investigation of the performance of a high pressure direct injection (HPDI) natural gas engine. In: Proceedings of the ASME 2014 Internal Combustion Engine Division Fall Technical Conference; Oct 19–22; Columbus, IN, USA.

Li G, Lennox T, Goudie D, Dunn M. 2005. Modeling HPDI natural gas heavy duty engine combustion. In: Proceedings of ICEF2005: ASME Internal Combustion Engine Division 2005 Fall Technical Conference; Sep 11–14 Sep; Ottawa, Canada.

Li M, Zhang Q, Li G. 2017. Effects of hydrogen addition on the performance of pilot-ignition direct-injection natural gas engine: a numerical study. Energy Fuels. 31:4407–4423.

Li M, Zhang Q, Li G, Shao S. 2015. Experimental investigation on performance and heat release analysis of a pilot ignited direct injection natural gas engine. Energy. 90:1251–1260.

MAN Diesel & Turbo. 2014. MAN B&W S60MC-C8.2 -TII Project Guide. No. 7020-0222-00ppr May 2014 Copenhagen, Denmark.

MAN Energy Solutions. 2015. CEAS engine data report 5S60ME-C8.5-GI (methane) with high load tuning. [accessed 2020 Dec 20]. https://marine.man-es.com/two-stroke/ceas.

McTaggart-Cowan GP, Munshi SR, Rogak SN, Hill PG, Bushe WK. 2007. Hydrogen-methane blend fuelling of a heavy-duty, direct-injection engine. In: Proceedings of IMECE2007: 2007 ASME International Mechanical Engineering Congress and Exposition; Nov 11–15; Seattle, Washington, USA.

McTaggart-Cowan GP, Rogak SN, Hill PG, Bushe WK, Munshi SR. 2004. Effects of operating condition on particulate matter and nitrogen oxides emissions from a heavy-duty direct injection natural gas engine using cooled exhaust gas recirculation. Int J Engine Res. 5(6):499–511.

McTaggart-Cowan GP, Rogak SN, Munshi SR, Hill PG, Bushe WK. 2010. The influence of fuel composition on a heavy-duty, natural-gas direct-injection engine. Fuel. 89(3):752–759.

Melte PC, Pratt DT. 1974. Measurement of atomic oxygen and nitrogen oxides in jet stirred combustion. Symp (Int) Combust. 15(1):1061–1070.

Murthy S. 1974. Turbulent mixing in non-reactive and reactive flows. Boston (MA): Springer.

Ott M. 2015. Low pressure gas engines. The industry standard. CIMAC discussion Athens. Jan 2015. http://www.lme.ntua.gr:8080/whats-new/news-1/03_MO.pdf.

Ouellette P. 1996. Direct injection of natural gas for the diesel engine fueling [dissertation]. Vancouver (CA): The University of British Columbia.

Ouellette P, Hill PG. 2000. Turbulent transient gas injections. J Fluids Eng. 122(4):743–754.

Patel A, Kong SC, Reitz RD. 2004. Development and validation of a reduced reaction mechanism for HCCI engine simulations. SAE Technical Paper Series. No. 2004-01-0558.

Peters N. 1984. Laminar diffusion flamelet models in non-premixed turbulent combustion. Prog Energy Combust Sci. 10:319–339.

Schwerdt C. 2006. Modelling NOx-formation in combustion processes [dissertation]. Scania (Sweden): Lund University.

Tao F, Reitz RD, Foster DE, Liu Y. 2007. Nine-step phenomenological diesel soot model validated over a wide range of engine conditions. Int J Therm Sci. 48:1223–1234.

Tsuboi T, Wagner HG. 1975. Homogeneous thermal oxidation of methane in reflected shock waves. Symp (Int) Combus. 15(1):883–890.

Wang Q, Shao C, Liu Q, Zhang Z, He Z. 2017. Effects of injection rate on combustion and emissions of a pilot ignited direct injection natural gas engine. J Mech Sci Technol. 31(4):1969–1978.

Yang R. 2018. CFD modelling and investigation of the marine dual-fuel two-stroke engine with gas high pressure direct admission [dissertation]. Glasgow (UK): University of Strathclyde.

Yang R, Theotokatos G, Vassalos D. 2020. Parametric investigation of a large two-stroke marine high-pressure direct injection engine by using computational fluid dynamics method. Proceedings of the institution of Mechanical engineers. Part M: J Eng Marit Environ. 234 (3):699–711.

Zhang Q, Li M, Shao S. 2015. Combustion process and emissions of a heavy-duty engine fuelled with directly injected natural gas and pilot diesel. Appl Energy. 157:217–228.